Robust Sub-Kelvin Simulations of Quantum Dot Charge Sensing

Raphaël J. Prentki*, Felix Fehse*†, Pericles Philippopoulos*, Chenyi Zhou*,
Hong Guo*†, Marek Korkusinski‡, and Félix Beaudoin*

*Nanoacademic Technologies Inc. (Montréal, QC, Canada)
†Department of Physics, McGill University (Montréal, QC, Canada)
‡Security and Disruptive Technologies Research Centre, National Research Council (Ottawa, ON, Canada)

***Abstract*—Spin-qubit-based quantum computing technologies commonly involve quantum point contacts (QPCs). Indeed, the conductance quantization exhibited by QPCs may be harnessed for the sensing of the charge in a quantum dot (QD) which may, in turn, be harnessed for spin-qubit characterization and readout. In this work, we report a self-consistent finite-element method (FEM) simulation scheme for QD charge sensing by a QPC in planar semiconductor heterostructures. This scheme fully accounts for the electrostatics, quantum confinement, and quantum transport phenomena that are relevant in semiconductor quantum wells (QWs). Robust sub-Kelvin convergence is achieved partly thanks to an adaptive meshing algorithm for Poisson's equation and partly thanks to the uncertainty principle, which leads to diffuse charge density profiles. To minimize computational burden, we leverage the quasi-separability of the Schrödinger equation in the QW, turning a 3D problem into a set of 1D problems; furthermore, we leverage the sub-Kelvin temperature to reduce the calculation of the QPC's conductance to a single Green's function evaluation. Finally, we report: (A) simulations of the hole density in an AlGaAs–GaAs QW accurately matching experimental data and (B) charge sensing in simulations of realistic QD and QPC devices, thereby demonstrating our simulation scheme's relevance to the modeling of spin qubit technologies.**

***Index Terms*—Finite-element method (FEM), technology computer-aided design (TCAD), nonequilibrium Green's function (NEGF) formalism, sub-Kelvin temperature, quantum computing, spin qubit, quantum dot, quantum point contact (QPC).**

I. Introduction

A quantum point contact (QPC) is a narrow constriction between two electrical conductors. Since the width of this constriction is on the order of the wavelength of charge carriers, QPCs exhibit conductance quantization [1], [2]. As a result, they can be used as charge detectors with sensitivity on the order of the elementary charge. For example, a QPC can be gated by an electron or hole confined within a neighboring quantum dot (QD). In systems with spin-to-charge conversion, QPCs can thus be used for readout of spin qubits [3]. More generally, QPCs can be used to characterize spin qubits [4]. To achieve practical simulations of a QPC gated by a QD, several elements are required: (A) the modeling of quantum confinement in the QD and QPC and its impact on charge transport, (B) the modeling of electrostatics, in particular the gating of the QPC by the QD, (C) robust convergence at sub-Kelvin temperature, a regime in which QD and QPC are typically operated for quantum-computing applications, and (D) low computational burden, due to the extreme sensitivity of the QPC's conductance on device geometry, material composition, and external voltages, which demands parameter fine-tuning to achieve charge sensing capability. In this work, we present a simulation framework satisfying these requirements implemented in the finite-element method (FEM) software package QTCAD® (Quantum Technology Computer-Aided Design) [5]–[8].

R. J. Prentki and F. Fehse contributed equally to this work. Contact emails: rprentki@nanoacademic.com (R. J. Prentki) and ffehse@nanoacademic.com (F. Fehse). The authors gratefully acknowledge financial support from the QSP 015 project within the "Internet of Things: Quantum Sensors Challenge" Program (QSP) of the National Research Council (NRC) of Canada.

II. Device structure

As a vehicle to this study, we consider the experimental device described in Ref. [4]. It consists of a two-dimensional hole gas (2DHG) formed within a quantum well (QW) across an $Al_{0.5}Ga_{0.5}As$–GaAs heterojunction [Fig. 1]; holes in GaAs are a promising platform for spin qubits due to their low coupling to nuclear spins, which is expected to lead to long coherence time [9], [10]. The heterojunction is undoped; electrically-stable nanostructures are typically difficult to fabricate in p-doped AlGaAs–GaAs heterostructures [11]. To attract holes within the QW, a large negative voltage V_{TG} is applied on the Al global top gate. 3D (2D) confinement is achieved in the QD (QPC) by applying voltages $> V_{\mathrm{TG}}$ on the Ti/Au gates located on the Al_2O_3–$Al_{0.5}Ga_{0.5}As$ interface [Fig. 2(a)]. For simulation purposes, the Al and Ti/Au gates are taken to have infinitesimal thickness; the GaAs layer is taken to be sufficiently thick so as to have vanishing displacement field on its bottom surface.

III. Quantum-well solver

The only charges in the device are holes confined within the QD and the rest of the QW. They are modeled within a four-band Luttinger–Kohn–Foreman $\boldsymbol{k}\cdot\boldsymbol{p}$ model [12], [13], in which the time-independent Schrödinger equation is

$$\left[\frac{\hbar^2}{2}\boldsymbol{k}^T\cdot\boldsymbol{D}\cdot\boldsymbol{k}+V(\boldsymbol{r})\right]\boldsymbol{F}(\boldsymbol{r})=E\boldsymbol{F}(\boldsymbol{r})\,, \tag{1}$$

where $\hbar$ is the reduced Planck constant, $\boldsymbol{k}=-i\boldsymbol{\nabla}=(k_x,k_y,k_z)$ is the crystal momentum, $\boldsymbol{D}$ is a generalization of the effective mass tensor which captures inter-band interactions and the discontinuity of the bandstructure along the heterostructure growth axis, $\boldsymbol{r}=(x,y,z)$ is the position, $\boldsymbol{F}(\boldsymbol{r})$ is the four-band envelope function, and E is its eigenenergy. Note that the elements of $\boldsymbol{D}$ may be written

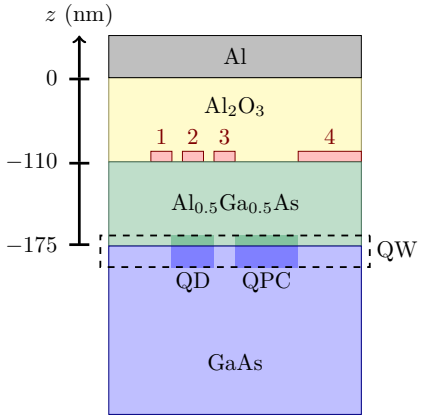

Fig. 1. Diagram of the heterostructure of the simulated device. The regions labeled by 1–3 (4) are Ti/Au gates used to achieve 3D (2D) confinement in the QD (QPC). (Not to scale.)

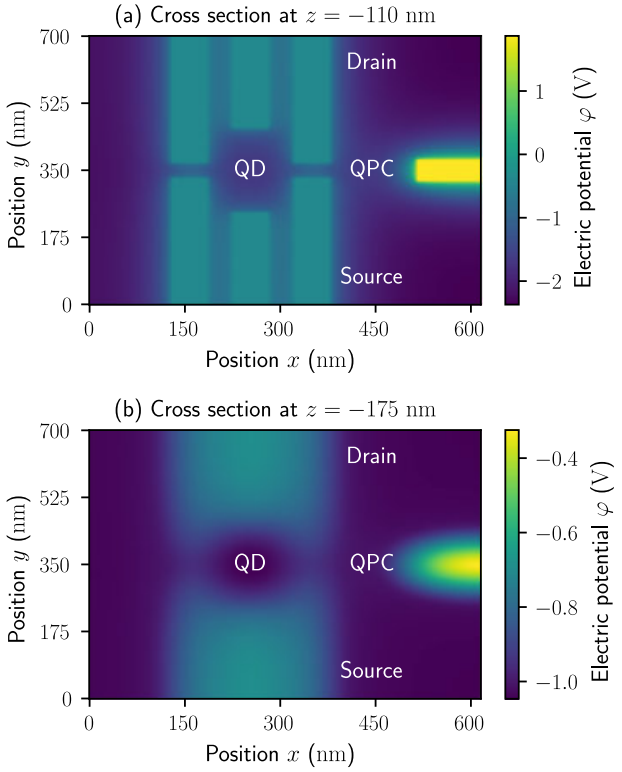

Fig. 2. Cross sections of the calculated electric potential on (a) the Al_2O_3–$Al_{0.5}Ga_{0.5}As$ interface, which highlights the layout of the Ti/Au gates used to achieve 3D (2D) confinement to form the QD (QPC), and (b) the $Al_{0.5}Ga_{0.5}As$–GaAs interface, which highlights the potential experienced by holes in the QW. The external voltages are compatible with the harboring of two holes by the QD and charge sensing by the QPC.

as $D_{nm}^{\alpha\beta}$, where α, β index the three Cartesian directions of momentum space and n, m index the four bands. Finally, $V(\boldsymbol{r})$ is the potential energy for holes:

$$V(\boldsymbol{r}) = q\left[\varphi(\boldsymbol{r}) - \varphi_{\mathrm{F}}\right] + \chi(\boldsymbol{r}) + E_{\mathrm{g}}(\boldsymbol{r})\,, \tag{2}$$

where $q > 0$ is the elementary charge, $\varphi(\boldsymbol{r})$ is the electric potential, φ_{F} is a reference potential, $E_{\mathrm{g}}(\boldsymbol{r})$ is the bandgap energy, and $\chi(\boldsymbol{r})$ is the electron affinity. The electric potential is obtained by solving Poisson's equation:

$$\boldsymbol{\nabla} \cdot \left[\varepsilon(\boldsymbol{r})\boldsymbol{\nabla}\varphi(\boldsymbol{r})\right] = -qp(\boldsymbol{r})\,, \tag{3}$$

where $\varepsilon(\boldsymbol{r})$ is the permittivity and $p(\boldsymbol{r})$ is the hole density.

In the QD, holes are 3D-confined, so that the hole density is given by

$$p_{\mathrm{QD}}(\boldsymbol{r}) = \sum_{n,i} \left|F_{n,i}(\boldsymbol{r})\right|^2 \frac{1}{1 + e^{\frac{E_i - E_{\mathrm{F}}}{k_{\mathrm{B}}T}}}\,, \tag{4}$$

where n is the band index, i indexes the bound states of the QD with four-band envelope functions $F_i(\boldsymbol{r})$ and eigenenergies E_i, E_{F} is the Fermi level (set to be $E_{\mathrm{F}} = 0$ in this work), k_{B} is the Boltzmann constant, and T is the temperature. Note that, for simplicity, hole–hole Coulomb interactions were ignored in Eq. (4).

Elsewhere in the QW, the calculation of the 3D hole density may be simplified to a set of 1D problems in the confinement direction z under the assumption of "quasi-separability", which requires that (A) $V(\boldsymbol{r}) \approx V_{xy}(x, y) + V_z(z)$ and (B) $D_{nm}^{\alpha\beta} = 0$ for all $n \neq m$. Condition (A) is justified by the much stronger confinement along z than along x and y. Condition (B) is formally false due to off-diagonal elements of the $\boldsymbol{D}$ tensor coupling k_z to k_x and k_y. However, a perturbation theory analysis indicated that these elements induce corrections to the hole density of at most $\approx 5\%$ compared to a calculation involving the diagonal elements of $\boldsymbol{D}$ only; we thus ignore these off-diagonal elements. Therefore, for each position (x, y), we solve a 1D Schrödinger equation:

$$\left[\frac{\hbar^2}{2} k_z \tilde{\boldsymbol{D}} k_z + V^{(x,y)}(z) - E^{(x,y)}\right] \boldsymbol{f}^{(x,y)}(z) = 0\,, \tag{5}$$

where the elements of $\tilde{\boldsymbol{D}}$ are given by $\tilde{D}_{nm} = D_{nm}^{zz}\delta_{nm}$, δ_{nm} is a Kronecker delta, $V^{(x,y)}(z)$ is the interpolation of $V(\boldsymbol{r})$ on a linecut parallel to the z axis crossing the QW at position (x, y), $\boldsymbol{f}^{(x,y)}(z)$ is the 1D four-band envelope function, and $E^{(x,y)}$ is its eigenenergy. Since $\tilde{\boldsymbol{D}}$ is diagonal, Eq. (5) is an effective-mass approximation. Figure 4(b) illustrates the solution to such a 1D Schrödinger equation. Having solved the 1D Schrödinger equations, under the assumption of quasi-separability, we can express the QW hole density on a given linecut (x, y) as

$$p_{\mathrm{QW}}^{(x,y)}(z) = \sum_{n,j} \left|f_{n,j}^{(x,y)}(z)\right|^2 \frac{m_n^\star k_{\mathrm{B}} T}{2\pi\hbar^2} \ln\left[1 + e^{\eta_{n,j}^{(x,y)}}\right]\,, \tag{6}$$

$$\eta_{n,j}^{(x,y)} = \left(E_{\mathrm{F}} - E_{n,j}^{(x,y)}\right) / (k_{\mathrm{B}}T)\,, \tag{7}$$

where $m_n^\star$ is the 2D density-of-states effective mass for band n (which may be computed from the elements of $\tilde{\boldsymbol{D}}$) and j indexes the eigenstates of Eq. (5).

We calculate the hole density $p_{\mathrm{QW}}^{(x,y)}(z)$ on sufficiently many linecuts (x, y) and then linearly interpolate the results to find the QW hole density $p_{\mathrm{QW}}(\boldsymbol{r})$ for any $\boldsymbol{r}$. Through careful optimization, the interpolations involved in this QW solver algorithm, namely (A) the interpolations from the 3D device mesh to the set of 1D linecut meshes (i.e. $V(\boldsymbol{r}) \to V^{(x,y)}(z)$), and (B) the interpolation from the set of 1D linecut meshes to the 3D device mesh (i.e. $p_{\mathrm{QW}}^{(x,y)}(z) \to p_{\mathrm{QW}}(\boldsymbol{r})$), can both be calculated in $\mathcal{O}(N)$ time, where N is the number of nodes on the target mesh. In our QW solver simulations, the 3D device mesh has $\approx 1.6 \times 10^6$ nodes, the 1D Schrödinger equations are solved

over $\approx 5.2 \times 10^3$ linecuts, and each 1D linecut mesh has 351 nodes. Finally, the total hole density is obtained through the sum $p(\boldsymbol{r}) = p_{\mathrm{QD}}(\boldsymbol{r}) + p_{\mathrm{QW}}(\boldsymbol{r})$; see Fig. 3 for the total hole density in the QW of the device investigated in this paper and Fig. 2(b) for the corresponding electric potential.

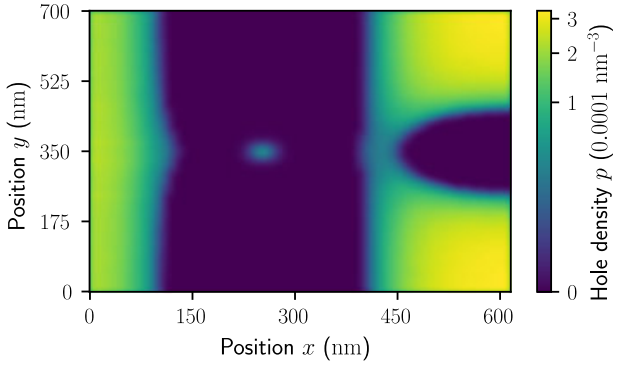

Fig. 3. Cross section of the calculated hole density on the $Al_{0.5}Ga_{0.5}As$–GaAs interface. The external voltages are compatible with the harboring of two holes by the QD and charge sensing by the QPC.

IV. Sub-Kelvin robustness

Note that the Poisson equation [Eq. (3)] and the QW hole density equation [Eq. (6)] (which is based on the Schrödinger equation) are coupled. They are thus solved iteratively until self-consistency is reached. The Schrödinger–Poisson iteration's initial guess is taken to be the solution to a classical nonlinear Poisson equation within the Thomas–Fermi approximation. Such equations are notoriously difficult to solve iteratively at cryogenic T, notably due to the "sharpness" of classical charge density profiles, which is exacerbated in the sub-Kelvin regime; see Fig. 4(a) and Refs. [14]–[16]. To resolve this issue, in a previous work, we demonstrated an adaptive meshing algorithm for the classical nonlinear Poisson equation, thereby enabling convergence down to sub-Kelvin temperatures [6]. Alternatively, if available, the initial guess is taken to be the solution to the coupled Schrödinger–Poisson equations for the same device at similar external voltages. The subsequent Schrödinger–Poisson iterations pose little convergence difficulties thanks to the uncertainty principle, which leads to more "diffuse" charge density profiles [Fig. 4(b)]. Note that except for the data of Fig. 5, throughout this work, we set $T = 100$ mK. With an initial guess based on the classical nonlinear Poisson equation, the Schrödinger–Poisson iterations converged in around 2.6 hours on a 64-core processor, despite our very dense meshes [Sec. III]; with an initial guess based on the QW solver, they converged around 7 times faster.

V. Comparison with experimental data

To calibrate our simulation parameters, we compare hole density calculations based on Eq. (6) to Hall resistivity measurements [17] in a bulk Al_2O_3–$Al_{0.5}Ga_{0.5}As$–GaAs heterostructure. We find that our simulations exhibit excellent agreement with experimental data [Fig. 5] provided that we use the experimental values of relative permittivity for Al_2O_3 and $Al_{0.5}Ga_{0.5}As$ quoted in Ref. [17] (7.2 and 11.5, respectively) and set the Al workfunction to 4.98 eV. Alternatively,

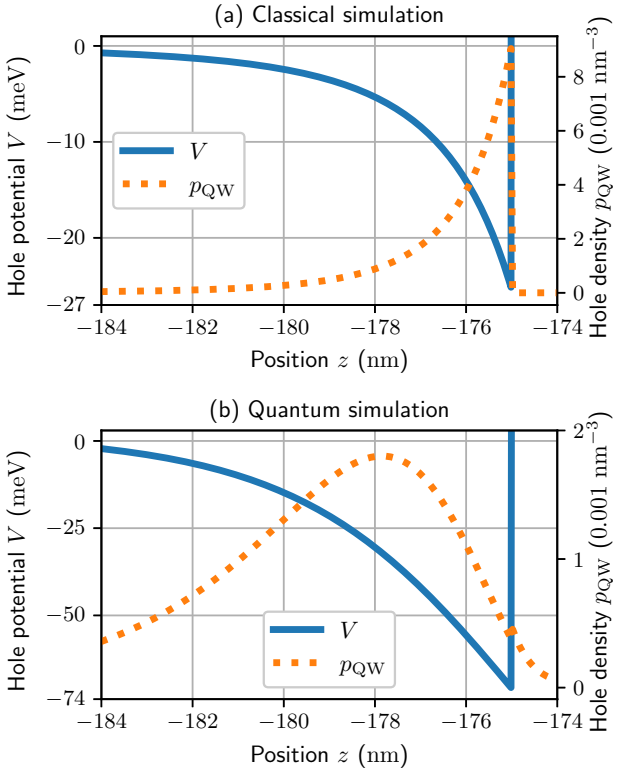

Fig. 4. Potential energy and hole density profiles in the heterostructure of Fig. 1, except without the Ti/Au gates, as obtained via simulations based on (a) the classical nonlinear Poisson equation and (b) the Schrödinger–Poisson equations.

the Al workfunction could have been set to a value closer to experimental data ($\approx$ 4.2 eV [18]) while introducing a negative sheet charge trapped in the Al_2O_3 layer.

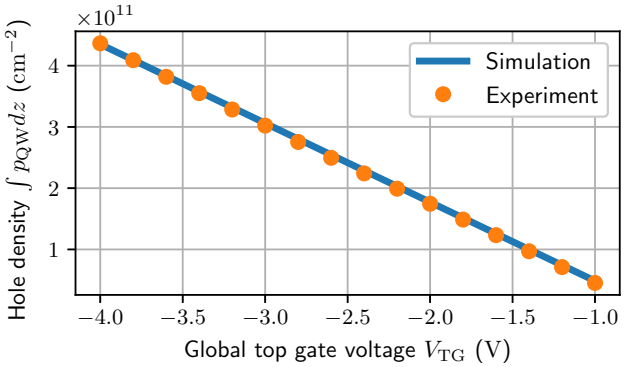

Fig. 5. 2DHG sheet charge density as a function of global top gate voltage for the same heterostructure as in Fig. 1, except without the Ti/Au gates, with an oxide thickness of 244 nm, and with an $Al_{0.5}Ga_{0.5}As$ thickness of 100 nm, at $T = 4$ K. The experimental data are taken from Fig. 1(c) of Ref. [17] while simulations are based on Sec. III.

VI. NEGF conductance and charge sensing

At equilibrium (i.e. when the source–drain voltage is 0), in the $T \to 0$ limit, the energy window for quantum transport through the QPC is limited to E_{F}. This applies to the sub-Kelvin regime we are investigating; we may thus compute the QPC conductance through

$$G = \frac{q^2}{h} \overline{T}(E = E_{\mathrm{F}}) \,, \tag{8}$$

where $h = 2\pi\hbar$ and $\overline{T}(E)$ is the transmission function in the two-probe system composed of the source, QPC constriction, and drain shown in Fig. 2(a). We compute $\overline{T}(E)$ using the nonequilibrium Green's function (NEGF) formalism assuming coherent transport [1], [19], [20], so that

$$\overline{T}(E) = \mathrm{Tr}\left[\Gamma_{\mathrm{D}}\mathcal{G}^{\mathrm{R}}\Gamma_{\mathrm{S}}\mathcal{G}^{\mathrm{A}}\right] , \tag{9}$$

where $\Gamma_{\mathrm{S,D}}$ is the source/drain broadening function and $\mathcal{G}^{\mathrm{R}} = \left(\mathcal{G}^{\mathrm{A}}\right)^{\dagger}$ is the retarded Green's function. This formalism naturally accounts for the 2D confinement and quantum interferences that arise in the QPC. Importantly, the calculation of G through Eq. (8) only requires a single NEGF evaluation.

Figure 6 shows the calculated QPC conductance as a function of QPC gate voltage V_{QPC}. As expected, the QPC exhibits conductance quantization. G transitions from 0 to $2q^2/h$ around $V_{\mathrm{QPC}} = 2.24$ V; as such, this particular value of V_{QPC} is well-suited to operate the QPC as a QD charge sensor. To demonstrate this, we compute the 3D-bound hole density in the QD using Eqs. (1) and (4) and find the QD holds a total charge of $2q$ [see Fig. 3]. Solving Poisson's equation [Eq. (3)], we find that this QD charge slightly increases the potential energy in the QPC channel [Eq. (2)], thereby reducing its number of conduction modes. Correspondingly, introducing a charge in the QD reduces G from $\approx 0.97q^2/h$ to $\sim 0.74q^2/h$ (see arrow in Fig. 6), thereby demonstrating the QPC's charge sensing capability.

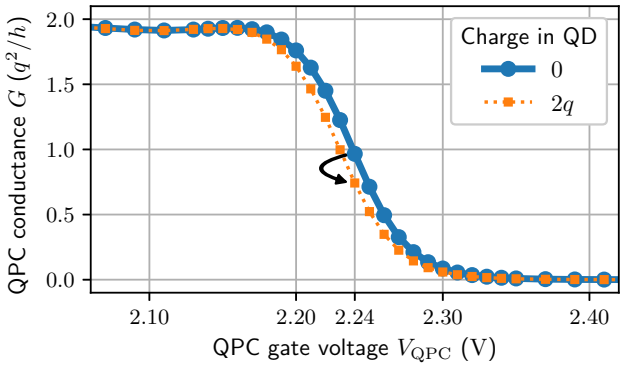

Fig. 6. Calculated QPC conductance–voltage characteristic with and without charge in the neighboring QD.

VII. Conclusion

We have demonstrated a simulation methodology for two ubiquitous quantum computing devices, namely the QDs and QPCs that may be found in semiconductor heterojunction QWs, and applied it to an experimental, undoped, hole-majority quantum device. By capitalizing on the quasi-separability of the Schrödinger equation in the QW and the narrow energy window for quantum transport, we kept computational burden to a minimum. Finally, through adaptive meshing and the uncertainty principle, we achieved robust simulation convergence, even in the sub-Kelvin regime.

References

[1] P. Havu, V. Havu, M. J. Puska, and R. M. Nieminen, "Nonequilibrium electron transport in two-dimensional nanostructures modeled using Green's functions and the finite-element method," *Physical Review B*, vol. 69, no. 11, p. 115325, Mar. 2004. DOI: 10.1103/PhysRevB.69.115325.

[2] A. Siddiki and F. Marquardt, "Self-consistent calculation of the electron distribution near a quantum point contact in the integer quantum Hall effect," *Physical Review B*, vol. 75, no. 4, p. 045325, Jan. 2007. DOI: 10.1103/PhysRevB.75.045325.

[3] B. M. Maune, M. G. Borselli, B. Huang, T. D. Ladd, P. W. Deelman, K. S. Holabird, A. A. Kiselev, I. Alvarado-Rodriguez, R. S. Ross, A. E. Schmitz, M. Sokolich, C. A. Watson, M. F. Gyure, and A. T. Hunter, "Coherent singlet-triplet oscillations in a silicon-based double quantum dot," *Nature*, vol. 481, no. 7381, pp. 344–347, Jan. 2012. DOI: 10.1038/nature10707.

[4] A. Bogan, S. Studenikin, M. Korkusinski, L. Gaudreau, J. Phoenix, P. Zawadzki, A. Sachrajda, L. Tracy, J. Reno, and T. Hargett, "Spin–orbit enabled quantum transport channels in a two-hole double quantum dot," *Physical Review B*, vol. 103, no. 23, p. 235310, Jun. 2021. DOI: 10.1103/PhysRevB.103.235310.

[5] https://nanoacademic.com/solutions/qtcad/.

[6] F. Beaudoin, P. Philippopoulos, C. Zhou, I. Kriekouki, M. Pioro-Ladrière, H. Guo, and P. Galy, "Robust technology computer-aided design of gated quantum dots at cryogenic temperature," *Applied Physics Letters*, vol. 120, no. 26, p. 264001, Jun. 2022. DOI: 10.1063/5.0097202.

[7] I. Kriekouki, F. Beaudoin, P. Philippopoulos, C. Zhou, J. C. Lemyre, S. Rochette, S. Mir, M. J. Barragan, M. Pioro-Ladrière, and P. Galy, "Interpretation of 28 nm FD-SOI quantum dot transport data taken at 1.4 K using 3D quantum TCAD simulations," *Solid-State Electronics*, vol. 194, p. 108355, Aug. 2022. DOI: 10.1016/j.sse.2022.108355.

[8] I. Kriekouki, F. Beaudoin, P. Philippopoulos, C. Zhou, J. C. Lemyre, S. Rochette, C. Rohrbacher, S. Mir, M. J. Barragan, M. Pioro-Ladrière, and P. Galy, "Understanding conditions for the single electron regime in 28 nm FD-SOI quantum dots: Interpretation of experimental data with 3D quantum TCAD simulations," *Solid-State Electronics*, vol. 204, p. 108626, Jun. 2023. DOI: 10.1016/j.sse.2023.108626.

[9] J. Fischer, W. Coish, D. Bulaev, and D. Loss, "Spin decoherence of a heavy hole coupled to nuclear spins in a quantum dot," *Physical Review B*, vol. 78, no. 15, p. 155329, Oct. 2008. DOI: 10.1103/PhysRevB.78.155329.

[10] V. Marton, A. Sachrajda, M. Korkusinski, A. Bogan, and S. Studenikin, "Coherence characteristics of a GaAs single heavy-hole spin qubit using a modified single-shot latching readout technique," *Nanomaterials*, vol. 13, no. 5, p. 950, Mar. 2023. DOI: 10.3390/nano13050950.

[11] B. Grbić, R. Leturcq, K. Ensslin, D. Reuter, and A. D. Wieck, "Single-hole transistor in p-type GaAs/AlGaAs heterostructures," *Applied Physics Letters*, vol. 87, no. 23, p. 232108, Nov. 2005. DOI: 10.1063/1.2139994.

[12] J. M. Luttinger and W. Kohn, "Motion of electrons and holes in perturbed periodic fields," *Physical Review*, vol. 97, no. 4, p. 869, Feb. 1955. DOI: 10.1103/PhysRev.97.869.

[13] B. A. Foreman, "Effective-mass Hamiltonian and boundary conditions for the valence bands of semiconductor microstructures," *Physical Review B*, vol. 48, no. 7, p. 4964, Aug. 1993. DOI: 10.1103/PhysRevB.48.4964.

[14] M. Kantner and T. Koprucki, "Numerical simulation of carrier transport in semiconductor devices at cryogenic temperatures," *Optical and Quantum Electronics*, vol. 48, p. 543, Nov. 2016. DOI: 10.1007/s11082-016-0817-2.

[15] M. N. Ericson, T. S. Humble, F. G. Curtis, and F. A. Mohiyaddin, "Simulation of silicon nanodevices at cryogenic temperatures for quantum computing," *Proceedings of the 2017 COMSOL conference in Boston, MA*, Oct. 2017.

[16] A. Beckers, F. Jazaeri, and C. Enz, "Cryogenic MOS transistor model," *IEEE Transactions on Electron Devices*, vol. 65, no. 9, pp. 3617–3625, Aug. 2018. DOI: 10.1109/TED.2018.2854701.

[17] L. A. Tracy, T. Hargett, and J. Reno, "Few-hole double quantum dot in an undoped GaAs/AlGaAs heterostructure," *Applied Physics Letters*, vol. 104, no. 12, p. 123101, Mar. 2014. DOI: 10.1063/1.4868971.

[18] R. M. Eastment and C. H. B. Mee, "Work function measurements on (100), (110) and (111) surfaces of aluminium," *Journal of Physics F: Metal Physics*, vol. 3, no. 9, p. 1738, Sep. 1973. DOI: 10.1088/0305-4608/3/9/016.

[19] S. Datta, *Electronic Transport in Mesoscopic Systems*. Cambridge University Press, 1997. DOI: 10.1017/CBO9780511805776.

[20] R. J. Prentki, M. Harb, C. Zhou, P. Philippopoulos, F. Beaudoin, V. Michaud-Rioux, and H. Guo, "Tunneling leakage in ultrashort-channel MOSFETs—From atomistics to continuum modeling," *Solid-State Electronics*, vol. 197, p. 108438, Nov. 2022. DOI: 10.1016/j.sse.2022.108438.